Phase imaging of transition from classical to quantum plasmonic couplings between a metal nanoparticle and a metal surface

Hui Wang[a,1], Hui Yu[b], Yan Wang[c,d], Xiaonan Shan[e], Hong-Yuan Chen[a,1], and Nongjian Tao[c,d,1]

[a]State Key Laboratory of Analytical Chemistry for Life Science, School of Chemistry and Chemical Engineering, Nanjing University, 210023 Nanjing, China; [b]Institute for Personalized Medicine, School of Biomedical Engineering, Shanghai Jiao Tong University, 200030 Shanghai, China; [c]Biodesign Center for Bioelectronics and Biosensors, Arizona State University, Tempe, AZ 85287; [d]School of Electrical, Energy and Computer Engineering, Arizona State University, Tempe, AZ 85287; and [e]Department of Electrical and Computer Engineering, University of Houston, Houston, TX 77204

Edited by Catherine J. Murphy, University of Illinois at Urbana–Champaign, Urbana, IL, and approved June 15, 2020 (received for review April 13, 2020)

When a metal nanoparticle is brought near to a metal surface within electron tunneling distance (∼1 nm), classical electromagnetic coupling between the nanoparticle and the metal is expected to transition to quantum coupling. We show that this transition can be observed as a drastic phase change in the surface plasmon resonance (SPR) images of the gold nanoparticles. We study the transition by controlling the distance between the nanoparticles and electrode surface, modeling the impact of the transition on the SPR image in terms of a phase shift and demonstrating detection of microRNA based on the transition from classical to quantum coupling. The work shows that the quantum coupling can be directly visualized in SPR, and the extremely sensitive dependence of the transition on distance leads to a biosensing principle with SPR.

phase transition | quantum plasmonic coupling | classical coupling | biosensing

Surface plasmon resonance (SPR) imaging is widely used for label-free detection and quantification of molecular binding (1–4). The development of SPR microscopy has enabled imaging of individual metallic nanoparticles (NPs) (5), providing new insights into electrocatalysis (6), photocatalysis (7), biosensing (8–12), and electron transport at the single-NP level (13). Metallic NPs exhibit local SPR, which is responsible for the distinct colors as measured by optical absorption spectroscopy (14, 15). Recent studies have revealed an interesting quantum effect in the nanojunction formed between two gold nanoparticles (AuNPs) or between single AuNP and a metal surface (5, 16, 17). When the nanojunction gap is within the depth of the evanescent field, tunneling can occur between the AuNP and the metal surface (18, 19). Reducing the gap to a few nanometers or less, electron tunneling takes place across the nanojunctions, which leads to a transition from the classical coupling to the quantum coupling (18, 20). This transition has been observed by optical absorption spectroscopy and electron energy loss spectroscopy of the metallic NPs (17, 21). Because SPR imaging of NPs arises from the coupling between the NPs and Au film, we anticipate that the transition will be revealed by the SPR images. Unlike the previous spectroscopy techniques, this approach images the dynamic process of transition, which offers more transient details for biosensing with high temporal–spatial resolution.

Here, we show that the classical-to-quantum transition can be directly observed by SPR, and it has a profound impact on the SPR images of AuNPs. We study the transition between the classical and quantum plasmonics by precisely controlling the distance between single AuNP and the Au film from a few hundred nanometers to subnanometers and determine the distance where the transition takes place. We describe the transition in terms of a phase shift in the plasmonic wave scattered by the AuNP. We further demonstrate that the quantum coupling induced by the phase shift is extremely sensitive to the AuNP-Au film distance, and this sensitive distance dependence enables the detection of microRNA molecule.

Results and Discussion

We excited a surface plasmonic wave on an Au film by directing *p*-polarized incident light from a super luminescent diode onto the Au film via a high numerical aperture (NA) objective (NA = 1.49) of an inverted optical microscope (Fig. 1*A*). Light scattered from the Au film is collected with the same objective and forms an image on a complementary metal-oxide-semiconductor (CMOS) camera. Surface plasmons are excited on the Au film by illuminating with the tuned appropriate incident angle, and the plasmonic signal is extremely sensitive to the distance change near the surface of the Au film. While many three-dimensional (3D) positioning techniques have been developed for depth sensing (e.g., 3D superresolution microscopy) (22, 23), plasmonic imaging provides a highly sensitive, label-free method to image the phase transition from the classical to quantum regime. This enables the possibility for dynamic observation when combining with SPR technique.

To study the coupling between the AuNP and the Au film, we linked 150-nm AuNPs to the film via an antibody-antigen-antibody sandwich assay (experimental details are in *Materials and Methods* and *SI Appendix*, Fig. S2). The specific antibody-antigen binding ensures that each AuNP is separated from the Au film by an insulator (antibody-antigen-antibody linker). Each AuNP scatters the surface plasmonic wave and produces a bright spot with parabolic fringes in the direction the plasmonic wave (vertical)

Significance

When a metallic nanoparticle is brought within the electron tunneling distance from a metal surface, quantum coupling between the nanoparticle and the surface is anticipated. We show that the quantum effect can be directly observed by imaging the nanoparticle with a high-resolution plasmonic microscope. Direct measurement of the transition in terms of a phase shift induced by the quantum coupling between a metal nanoparticle and a metal surface opens prospective for a biosensing principle with surface plasmon resonance imaging.

Author contributions: H.W. and N.T. designed research; H.W. performed research; H.Y., X.S., and H.-Y.C. contributed new reagents/analytic tools; H.W. and Y.W. analyzed data; and H.W. wrote the paper.

The authors declare no competing interest.

This article is a PNAS Direct Submission.

Published under the PNAS license.

[1]To whom correspondence may be addressed. Email: huiwang520@nju.edu.cn, hychen@nju.edu.cn, or njtao@asu.edu.

This article contains supporting information online at https://www.pnas.org/lookup/suppl/doi:10.1073/pnas.2006443117/-/DCSupplemental.

First published July 14, 2020.

Downloaded at Palestinian Territory, occupied on December 12, 2021

www.manaraa.com

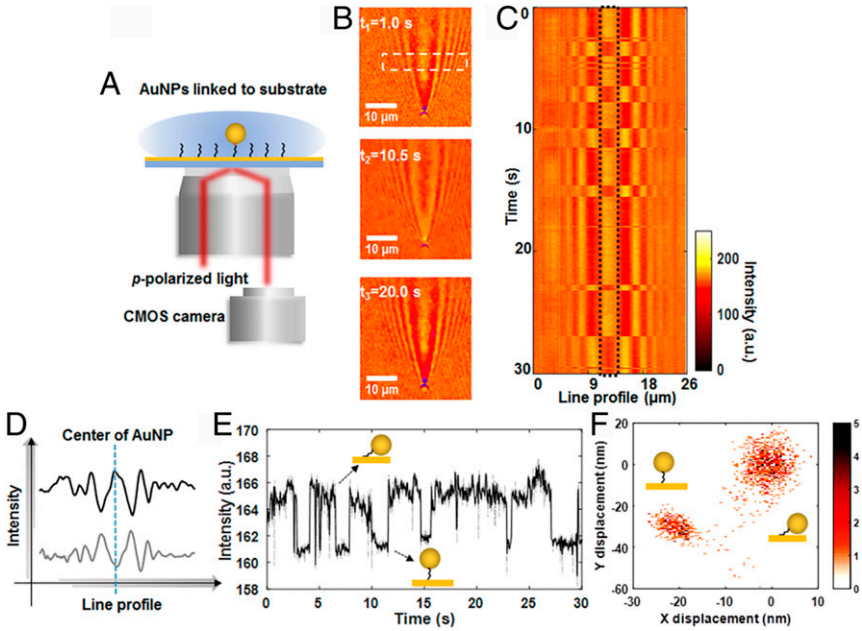

Fig. 1. Switching between the classical and quantum couplings of AuNPs linked to the Au film. (*A*) Schematic illustration of SPR imaging of the AuNPs linked to the Au film via the human PCT antibody–antigen–antibody sandwich assay. (*B*) Two distinct SPR images are detected: one with a dark-centered parabolic pattern, corresponding to the classical coupling regime, and the other one with a bright-centered pattern, corresponding to the quantum coupling regime. (Scale bars: 10 μm.) (*C*) The 2D line profile of the pattern (white dashed rectangle in *B*) vs. time. (*D*) Line profiles showing opposite phases of the two distinct patterns, where the vertical blue dashed line marks the center of the images. (*E*) Intensity of the center region (black dashed rectangle in *C*) of single AuNP vs. time, where the cartoons illustrate the AuNP-Au film distance change associated with the orientational change. Frame rate: 100 frames per second (fps). (*F*) Lateral positions (*x* and *y* directions) reveal two clusters associated with the two distinct states (patterns). AuNP diameter: 150 nm; a.u., arbitrary unit.

(Fig. 1*B*). This is the characteristic SPR image of an NP and has been observed previously (5, 24). However, a surprising observation in the present system is the random switching of the SPR image back and forth between two distinct patterns, one with a bright center and the other one with a dark center. Fig. 1*B* shows a few snapshots of the switching events, and Movie S1 provides more clear views of the switching events. Line profiles of the SPR images in the horizontal direction reveal oscillations, and the two distinct patterns have different phases (Fig. 1*D*).

The time dependence of the switching is illustrated by the intensity profile of a rectangular region marked in Fig. 1*B* (line profile in Fig. 1*C*). The average intensity at the center region (black dashed rectangle in Fig. 1*C*) of the parabolic pattern is plotted in Fig. 1*E*. We attribute the switching of the plasmonic image to the distance fluctuation between the NP and the Au film, which is introduced by the orientation variation of the linker (carton illustration of Fig. 1*E*). The lateral positions (*x* and *y*) of the AuNP reveal two main clusters separated by ∼25 nm, corresponding to the two orientations of the AuNP, which supports the conclusion (Fig. 1*F*). The distance change leads to the switching between the classical and quantum coupling regimes.

To validate the above observations, we studied the collision of bare AuNPs (without antibody coating) onto Au film. Fig. 2 *A*–*D* shows a few snapshots of single AuNP during colliding to the film. When the AuNP-film distance is far greater than the decay distance of the evanescent wave (∼200 nm), there is little coupling between the AuNP and the Au film, and the SPR image shows no contrast of the AuNP (Fig. 2*A*). When the AuNP enters the evanescent field, electromagnetic coupling takes place, and the parabolic SPR image pattern of the AuNP begins to emerge. The SPR image in this regime has a dark center (Fig. 2*B*). As the AuNP moves closer to the film, the image contrast continues to increase. However, the image pattern (dark center) changes little (Fig. 2*C*). This increase in the image contrast is expected because the evanescent field varies with the distance (d) as $\sim\exp(-d/L)$, where L is the evanescent field decay distance (∼200 nm) (25). The exponential dependence allows us to estimate the distance between the AuNP and the film surface.

Movie S2 reveals that the AuNP hits and sticks to the Au film surface during the collision process. Eventually, an abrupt change in the image pattern occurs with the dark center switching to bright (Fig. 2*D*). This AuNP collision measurement indicates that the phase of the SPR image switches when the AuNP hits to the Au film surface. The line profiles show the phase switching of the SPR images more clearly as the AuNP moving toward the Au film (Fig. 2*E*). Performing the same measurement with insulating NPs (e.g., polystyrene NPs) shows no phase switching in the SPR images during the collision process (*SI Appendix*, Fig. S3 and Movie S3). This experiment demonstrates that the phase switching is related to the metallic properties of AuNPs.

To further validate the above observation and determine the distance between the AuNP and the Au film at which the transition takes place, we controlled the distance by coating the Au film with n-alkanethiol (abbreviated as Cn) monolayers with different lengths (n) (*SI Appendix*, Fig. S1). Cn monolayers often have defects, which will affect the actual AuNP-Au film distance if the AuNPs are located in the defect regions. We examined the quality of the Cn monolayers by performing interfacial capacitance measurement. The data show capacitive charging effect, allowing us to determine the thicknesses of the Cn monolayers from the capacitance values. For 1-octadecanethiol (C18; thickness of 2.6 nm) (*SI Appendix*, Fig. S1), the SPR image of the AuNP has a dark center (Fig. 3*A*). When the monolayer thickness decreases, the SPR image switches from the dark-centered to the bright-centered patterns (Fig. 3*A*). The transition takes place around 1-hexanethiol (C6) (Fig. 3*B* and *SI Appendix*, Fig. S8), corresponding to thicknesses of ∼0.77 nm. We further measured the fluctuation of single AuNP on 1-hexanehexol-modified Au surface, which also reveals

Downloaded at Palestinian Territory, occupied on December 12, 2021

المنارة للاستشارات
www.manaraa.com

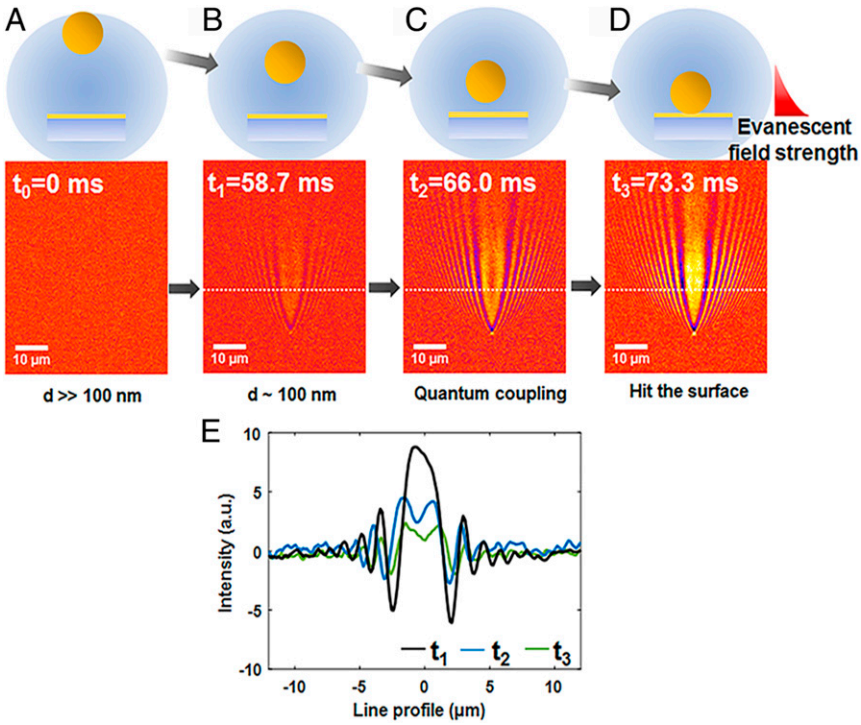

Fig. 2. Plasmonic images of single AuNP during the collision process with a bare Au film. (*A–D*) Snapshots of AuNP captured during the collision process, showing increasing contrast as the AuNP moves toward to the Au film and then sudden switching of the image from dark-centered to bright-centered patterns when the AuNP hits the surface. (Scale bars: 10 μm.) (*E*) Line profiles along the white dashed lines in *B–D* showing the phase shift in the plasmonic pattern. AuNP diameter: 60 nm. Frame rate: 409 fps. a.u., arbitrary unit.

the switching between the classical (dark) and the quantum coupling regimes (bright) in *SI Appendix*, Fig. S4. Characterizing the scattering of NP-thin film coupled systems (particle-on-mirror geometries) has been employed to analyze the wavelength shifts and polarization properties. While the scattering images feature an interesting doughnut-shaped point spread function with *s*-polarized incident light (25, 26), in our approach, *p*-polarized incident light is applied to excite the plasmonic wave and induces the parabolic pattern of single NP.

The maximum thickness of the Cn monolayer is a few nanometers (C18). To extend the distance between the AuNPs and the Au film, we deposited a 102-nm Cytop layer on the Au film. Cytop is chosen because it is an insulator and has a refractive index of 1.34, close to that of water, which preserves the SPR condition. The SPR image of 60-nm AuNPs shows the dark-centered SPR patterns (*SI Appendix*, Fig. S7). Because electron tunneling is negligible (27) at such long distance, only the classical electromagnetic coupling exists. This experiment further confirms that the dark-centered image corresponds to the classical coupling.

The experiments described above have demonstrated that the SPR image of single AuNP is highly sensitive to the distance between the NP and the Au film. When the distance is much larger than the decay distance of the evanescent field, there is no detectable image contrast. Decreasing the distance to a few hundreds of nanometers, the plasmonic image of AuNP begins to emerge, which has a parabolic pattern with a dark center. Further decreasing the distance below ~1 nm leads to the SPR image switching from the dark-centered pattern to a bright-centered pattern. This switching is abrupt, taking place within the subnanometer regime.

SPR imaging mechanism of single AuNP is the interference between a planar plasmonic wave excited by the incident light and a circular plasmonic wave associated with the scattering of the AuNP. The plasmonic image of the AuNP can be described by the following simplified expression (28),

$$I \sim Re\left\{E_{sp}(r)\alpha E_{sp}(r')e^{-i\kappa|r-r'|}\right\}, \quad [1]$$

where $E_{sp}(r)$ represents the planar plasmonic wave at position r, $\alpha E_{sp}(r')e^{-i\kappa|r-r'|}$ is the scattered wave by the AuNP at position r', α is the polarizability of the AuNP, and κ is the plasmonic wave number.

Eq. **1** shows that the SPR image of the AuNP depends on α, which is related to the optical response of the AuNP. For single AuNP far away from the Au film, α is given by

$$\alpha(\omega) = 4\pi\varepsilon_m a^3 \frac{\varepsilon(\omega) - \varepsilon_m}{\varepsilon(\omega) + 2\varepsilon_m}, \quad [2]$$

where a is radius of the AuNP, ε_m is the dielectric constant of the surrounding medium, and $\varepsilon(\omega)$ is the dielectric constant of the AuNP, which is a complex number and its frequency (ω) dependence determines the optical absorption spectra of the AuNP. Optical and electron energy loss spectra have revealed that when a metallic NP is within the electron tunneling distance from a metal surface or another metallic NP, $\varepsilon(\omega)$ changes dramatically. It leads to a local SPR mode and changes the polarizability, $\alpha(\omega)$. If we express α as $|\alpha|e^{i\delta}$, where $|\alpha|$ is the amplitude and δ is the phase, both will change with the transition from the classical to quantum coupling regime. Previous studies have shown that the plasmonic resonance peak has a red shift in wavelength when the transition occurs (25, 26). Compared with our excitation light of 680 nm, this indicates a sign change of the real part of polarizability and reverses the phase of the spherical wave component in Eq. **1** of AuNPs. Phase determines the qualitative feature of the SPR image pattern, and its change due to the

Downloaded at Palestinian Territory, occupied on December 12, 2021
www.manaraa.com

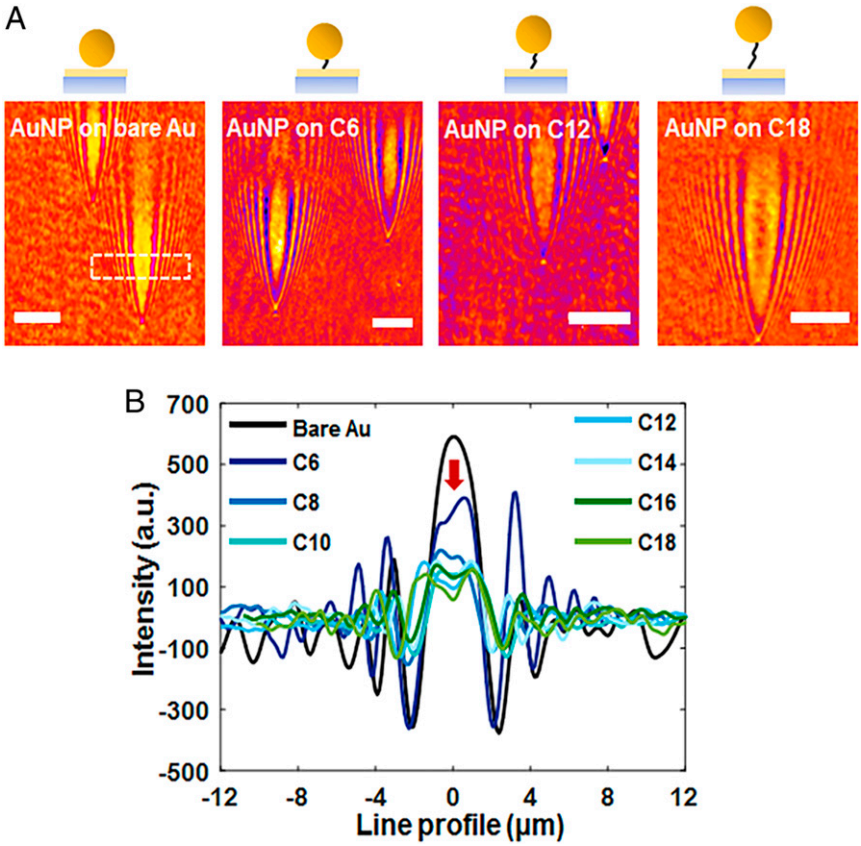

Fig. 3. Plasmonic images of 60-nm AuNPs on the Au film coated with different molecular lengths of alkanethiols. (*A*) Plasmonic images of AuNP on bare Au and C6- (1-hexanethiol), C12- (1-dodecanethiol), and C18-modified (1-octadecanethiol) Au substrates. (*B*) Intensity profiles (dashed rectangular region in *A*) showing changes in the phase with the distance between the AuNPs and the Au film (controlled by the molecular lengths). The largest change occurs when the distance is reduced to ∼0.77 nm (the thickness of the C6 layer). a.u., arbitrary unit. (Scale bars: 10 μm.)

transition is more sensitive. We simulated the SPR images of AuNP and its dependence on the phase shift using Eq. **1** and found that the phase shift leads to switching of the SPR image from dark-centered to bright-centered patterns (Fig. 4).

A distinct difference between the classical electromagnetic coupling and the quantum coupling is that the latter involves electron transfer between the AuNP and Au film. The timescale of the electron transfer is $\sim RC$, where R is the resistance of the AuNP–Au film nanojunction and C is the capacitance of the nanojunction. If RC is comparable with the plasmonic oscillation period $\sim 1/\omega_p$, where ω_p is the plasmon angular frequency ($\sim 2.7 \times 10^{15}$ rad/s) (29), then the electron transfer effect becomes significant, which makes the quantum coupling visible in the SPR image. The capacitance of single AuNP on a Cn monolayer-covered Au film is given by $C = \varepsilon\varepsilon_0 A/d$, where ε is the dielectric constant of the Cn monolayer at the plasmon resonance frequency, given by n^2 (n is the refractive index), and $\varepsilon_0 = 8.85 \times 10^{-12}$ F/m is the vacuum permittivity. The nanojunction conductance is given by $G_{total} = NG$, where N is the number of molecules bridged between the AuNP and Au film and G is the conductance per molecule. The classical-to-quantum transition takes place at $C/G_{total} \sim 1/\omega_p$, from which we have $G = A\frac{\epsilon\epsilon_0}{d}\omega_p$, where A is the contact area between the AuNP and the film. Assuming $A \sim 25$ nm^2 and $d \sim 1$ nm (17, 30, 31), the nanojunction conductance at which the transition takes place is $\sim 10^{-3}$ S or 13 G_0, where $G_0 = 77.4$ μS is the quantum conductance. This result is consistent with the optical extinction spectroscopy measurements (*SI Appendix*, Fig. S12), and the results are reported in the literature (32, 33). The spectra of single AuNP on different surfaces show different behaviors, which can distinguish the classical and quantum coupling situations.

The evanescent field in SPR decays exponentially from the surface of the Au film with a decay length of ∼200 nm. The high sensitivity of this imaging technique offers the opportunity for molecular binding detection with the receptors immobilized on the Au film. Electron tunneling also decays exponentially much faster than the evanescent field with a decay length ∼0.1 nm. This makes the SPR image phase extremely sensitive to the distance change in the quantum coupling regime and opens a way to detect small molecules. To demonstrate this capability, we performed microRNA detection (Fig. 5). We selected microRNA due to its importance for the molecular diagnosis of various diseases (34–36). MicroRNA-203 studied here can be found in almost all organs except for skin and esophagus.

To detect microRNA-203, 100-nm AuNPs modified with complementary single-strand DNA (ssDNA) with 25 nucleotides are immobilized on Au film. The estimated distance between the AuNPs and Au film is ∼10 nm, which is the classical coupling regime, and the SPR images of the AuNP are dark centered. microRNA-203 molecules are introduced to hybridize with the ssDNA. Duplex-specific nuclease (DSN) is then added to selectively digest ssDNA in the ssDNA:microRNA duplex, which decreases the distance between the AuNPs and the Au film. This leads to the transition from the classical to quantum regime, which is revealed by the switching from dark-centered to bright-centered SPR images of the AuNPs, indicating a large phase change (Fig. 5*A*, *Insets*). Before digestion of the ssDNA, substantial thermal fluctuations are detected in the lateral positions (x and y) of the AuNP in Fig. 5*B*, which is expected because each

CHEMISTRY
Downloaded at Palestinian Territory, occupied on December 12, 2021
www.manaraa.com

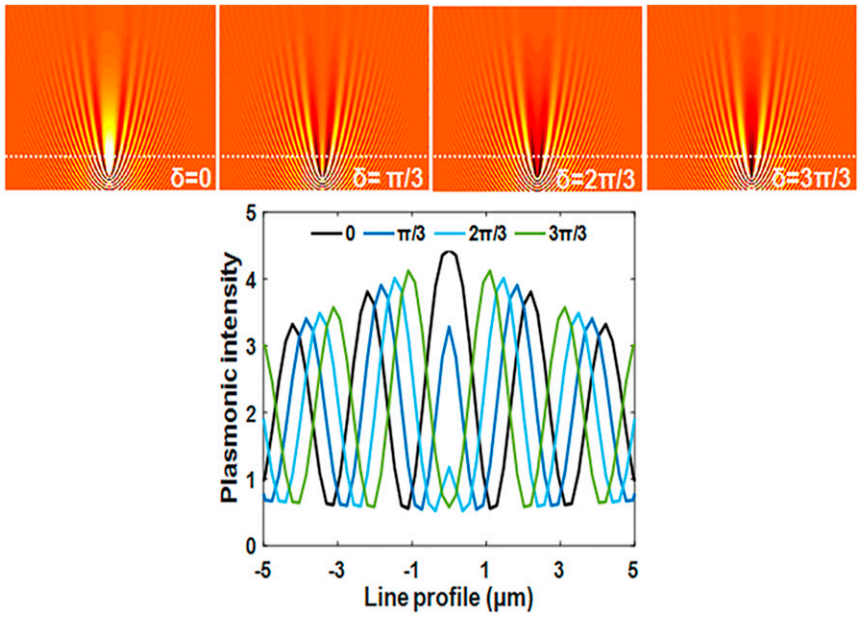

Fig. 4. Simulated SPR images and line profiles along the white dashed line of AuNP using Eqs. **1** and **2** for different phase shifts (δ).

AuNP linked by the ssDNA:microRNA duplex is still subjected to orientational motion (Fig. 5*C*) (37). After digestion, the thermal fluctuations are significantly reduced, indicating that the AuNPs are stuck to the Au film.

The time dependence of the ssDNA digestion is monitored by plotting the intensity at the center of the SPR images of AuNPs, revealing transition from dark- to bright-centered SPR images (Fig. 5*D* and Movie S4). To confirm the specific detection of the microRNA, we performed a control experiment using single-base mismatch microRNA. The control experiment shows no obvious phase change of the SPR images (Fig. 5*E*). Time lapse between the introduction of DSN and the phase change of the SPR images varies for different AuNPs, and the average time is 10.3 s as shown in Fig. 5*F*.

Conclusions

In conclusion, SPR images of the AuNPs are sensitive to the distance between the NPs and the Au film. When the distance is large (from a few hundred to a few nanometers), classical electromagnetic coupling dominates. When the distance is reduced to ~1 nm, a large phase change of the SPR image indicated the transition from the classical coupling regime to a quantum coupling regime, and then, electron transfer between the NPs and the Au film takes place. We further show that this classical-to-quantum transition enables the detection of microRNA molecules. This work also points to an approach to study charge transport in molecular junctions, which is proved to be a central task in molecular electronics and in the understanding of redox and catalytic reactions of molecules (38).

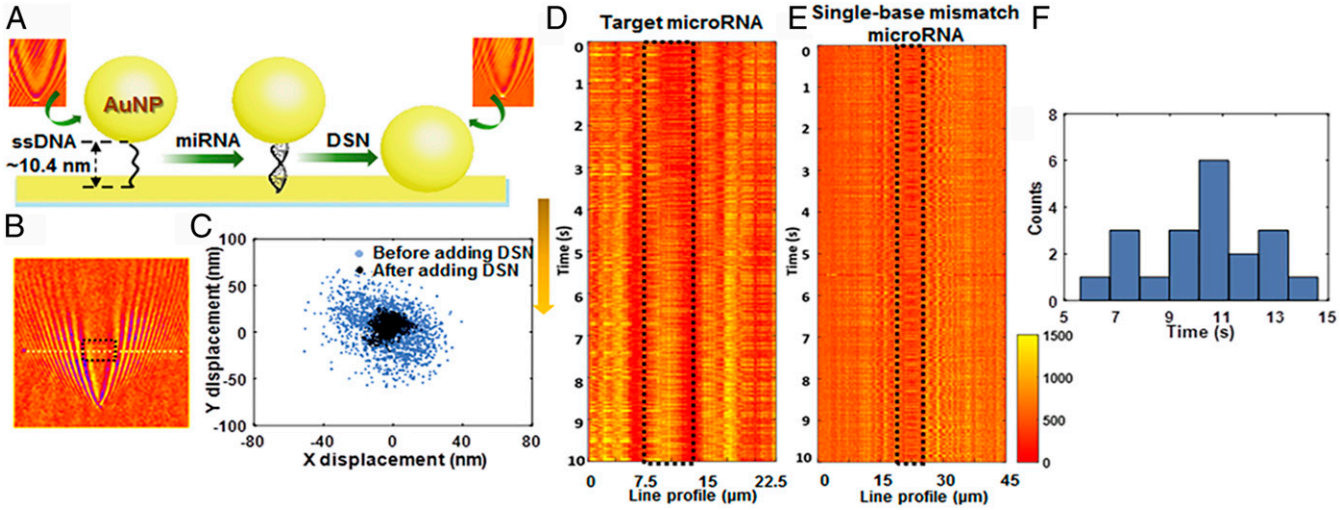

Fig. 5. MicroRNA detection based on the sharp transition from the classical to quantum coupling regimes. (*A*) Schematic illustration of microRNA detection using AuNPs coated with ssDNA. After hybridization with target microRNA and incubation with DSN, the ssDNA is cleaved, leading to a large reduction in the AuNP-Au film distance, and observed by the distinct switching in the phase of the SPR images. (*B*) SPR image of single AuNP. (*C*) Lateral displacement (*x* and *y* directions) of the AuNP shown in *B* before (blue dots) and after (black dots) adding DSN. (*D*) Line profile of AuNPs over time showing the cleavage process of the target microRNA:ssDNA hybridization. (*E*) Line profile of AuNPs over time for single-base mismatch microRNA:ssDNA hybridization incubating with DSN. (*F*) Distribution of DSN clearage time for different AuNPs. AuNP diameter: 100 nm.

Downloaded at Palestinian Territory, occupied on December 12, 2021
www.manaraa.com

Materials and Methods

Chemicals. Phosphate buffer solution (1×; 154 mM NaCl, 5.6 mM Na_2HPO_4, and 1.1 mM KH_2PO_4) was purchased from Corning Cellgro; 11-mercaptoundecanoic acid (11-MPA) was purchased from Adamas Reagent Co., Ltd. *N*-ethyl-*N*′-(3-dimethylaminopropyl) carbodiimide hydrochloride (EDC), *N*-hydroxysuccinimide (NHS), and bull serum albumin (BSA) powder were purchased from Sigma-Aldrich. Cytop (CTL809 from AGC Chemicals) was diluted with provided buffer (1:4 vol/vol) before using. Cn ($n = 6$, 10, 12, and 18) was purchased from Aladdin Industrial Corporation. Cn ($n = 8$ and 16) was purchased from Adamas Reagent Co., Ltd. Cn ($n = 14$) was purchased from Tokyo Chemical Industry Co. Ltd. All experiments were performed at room temperature.

Bare AuNPs with different diameters ($d = 60$ and 100 nm) were purchased from Nanopartz; 100-nm polystyrene NPs solution was purchased from Janus New-materials, and 150-nm AuNPs functionalized streptavidin solution from Nanopartz was diluted in deionized water (18 MΩ·cm, Milli-Q; Millipore Corp.). Human Procalcitonin (PCT) DuoSet ELISA kit (catalog no. DY8350-05) and DuoSet ancillary reagent kit 2 (catalog no. DY008) were purchased from R&D Systems.

All of the ssDNA and microRNA samples were purchased from Integrated DNA Technologies and received as lyophilized pellets in microcentrifuge tubes. The pellets were centrifuged to make sure that no residue was on the walls and then suspended in deionized water (Smart2Pure 3 UF; Thermo Fisher). The solution for ssDNA and microRNA hybridization was prepared by dissolving 10 mM $MgCl_2$ and 100 mM NaCl in 10 mM Tris·HCl buffer (pH 7.4). The ssDNA and microRNA sequences are as follows:

ssDNA: 5′-CTA GTG GTC CTA AAC ATT TCA CTT T-$(CH_2)_3$-SH-3′;

microRNA-203: GUG AAA UGU UUA GGA CCA CUA G;

single-base mismatch microRNA: GUG AAA UGU UUU GGA CCA CUA G.

An enzyme called DSN was purchased from Evrogen and received as a lyophilized enzyme in tubes. The DSN sample was diluted in the DSN storage buffer provided (5 μL buffer for each 10 U DSN) and incubated at 35 °C for 5 min after being gently vortexed.

Au Film Preparation.

1) Bare Au films preparation. Au films were prepared by vacuum evaporation technology; 2-nm Cr and 47-nm Au layers were coated on the BK-7 glass slides cleaned by acetone and then followed by deionized water.
2) Surface modification with alkanethiol. Au films were immersed in 5 mM alkanethiol/ethanol solution overnight, then rinsed with ethanol, and finally dried with nitrogen gas.
3) Surface modification of PCT detection. Au films were immersed in 1 mM 11-MPA/ethanol mixture overnight, rinsed with ethanol, and dried with nitrogen gas. The NHS/EDC mixture solution (mass ratio = 1:4) was added to the Au films for 20 min for activation of 11-MPA surface. The capture antibody was added to bind with the activated sites of 11-MPA. After washing three times with phosphate buffer solution with Tween (PBST) buffer, 100 μL standard PCT solution was added to the cell and incubated for 10 min, followed by adding 100 μL biotinylated PCT detection antibody solution for incubation over 10 min. One percent (wt/vol) BSA was then added to the cell for 10 min to block the residual activated sites on the surface; 50 μL 0.05% Tween 20 was added to the cell for further reduction of nonspecific binding, and finally, 50-μL AuNPs coated with streptavidin were added to the cell and captured by detection antibody molecules.
4) Cytop coating. Cytop (CTL809 from AGC Chemicals) was diluted with provided buffer (1:2 ∼ 1:4) before using; then, it was spin coated on top of the Au films (500 rpm for 20 s and then, 4,000 rpm for 20 s) and dried for 12 h.
5) Gel electrophoresis analysis. To confirm the hybridization of the ssDNA and microRNA-203 (or single-base mismatch microRNA), 12% denaturing polyacrylamide gel electrophoresis was employed here; 2 μM immobilized DNA and 2 μM miRNA-203 were incubated at 37 °C for 1 h and then loaded on the gel. Electrophoresis was carried out in 1× electrophoretic buffer solution (TBE) buffer at 150 V for 45 min at 25 °C. After separation, the gel was stained by ethidiumbromide and imaged with the fluorescence gel imaging system (*SI Appendix*, Fig. S9).

Optical Instruments and Data Analysis. The plasmonic imaging setup was built with an inverted microscope (Nikon Ti-E) and a 60× high-NA oil-immersion objective. A 680-nm super luminescent light-emitting diode (Q-photonics; operating power of 0.2 mW) was used as the light source. A polarizer was inserted in the optical path to generate *p*-polarized light to excite the surface plasmonic wave on the surface. For high-temporal resolution imaging, a low-noise CMOS imager (ORCA-Flash 4.0) was used. Atomic force microscope images of the samples were captured in solution with silicon nitride tips operated in contact mode (Agilent Technologies AFM 5500) to measure the roughness of the thiol-modified Au surfaces (*SI Appendix*, Fig. S11). The scanning electron microscopy characterization of AuNPs was carried out by JSM-7800F (*SI Appendix*, Fig. S10). Dynamic light scattering measurement of different NPs was performed to access the size distribution (*SI Appendix*, Fig. S10). All data processing steps were performed by Matlab software and Image J.

To examine the effects of focus and incident angle on the SPR images of AuNPs, we adjusted the two factors separately (*SI Appendix*, Figs. S5 and S6). To ensure the consistency and sensitivity of the SPR images, we performed all experiments with condition of the same plane ($z = 0$) and incident angle ($\theta < \theta_R$).

Single-NP Displacement Tracking in *x* and *y* Directions. To track the single-NP *x* and *y* positions from the plasmonic images, we developed an algorithm that can identify the plasmonic patterns of the individual NP and then determine the displacements along *x* and *y* directions in our recent publication (37). The rough *x* and *y* positions of a single NP are first determined based on two-dimensional (2D) correlation with pixel-level precision. The intensity profiles along *x* and *y* directions for each NP are then extracted and fitted with the polynomial function to calculate the exact position with subpixel precision (∼2.5 nm).

Data Availability. *SI Appendix* and Movies S1–S4 provide experimental data and parameter estimates.

ACKNOWLEDGMENTS. We thank Wei Wei for scanning electron microscopy measurement, Ben Niu and Hua Su for optical extinction measurements, and Yujiao Peng for gel electrophoresis detection. Financial support of this work was through National Natural Science Foundation of China Grants 21773117 and 21904062, Excellent Research Program of Nanjing University Grant ZYJH004, and Fundamental Research Funds for the Central Universities Grant 14380234.

1. J. Homola, Present and future of surface plasmon resonance biosensors. *Anal. Bioanal. Chem.* **377**, 528–539 (2003).
2. K. S. Phillips, Q. Cheng, Recent advances in surface plasmon resonance based techniques for bioanalysis. *Anal. Bioanal. Chem.* **387**, 1831–1840 (2007).
3. J.-F. Masson, Surface plasmon resonance clinical biosensors for medical diagnostics. *ACS Sens.* **2**, 16–30 (2017).
4. X. L. Zhou, Y. Yang, S. Wang, X. W. Liu, Surface plasmon resonance microscopy: From single-molecule sensing to single-cell imaging. *Angew. Chem. Int. Ed.* **59**, 1776–1785 (2020).
5. Y. Fang *et al*., Plasmonic imaging of electrochemical reactions of single nanoparticles. *Acc. Chem. Res.* **49**, 2614–2624 (2016).
6. X. Shan *et al*., Imaging the electrocatalytic activity of single nanoparticles. *Nat. Nanotechnol.* **7**, 668–672 (2012).
7. Y. Fang *et al*., Intermittent photocatalytic activity of single CdS nanoparticles. *Proc. Natl. Acad. Sci. U.S.A.* **114**, 10566–10571 (2017).
8. S. Wang *et al*., Label-free imaging, detection, and mass measurement of single viruses by surface plasmon resonance. *Proc. Natl. Acad. Sci. U.S.A.* **107**, 16028–16032 (2010).
9. W. Wang *et al*., Label-free measuring and mapping of binding kinetics of membrane proteins in single living cells. *Nat. Chem.* **4**, 846–853 (2012).
10. W. Wang *et al*., Single cells and intracellular processes studied by a plasmonic-based electrochemical impedance microscopy. *Nat. Chem.* **3**, 249–255 (2011).
11. Y. Yang *et al*., Interferometric plasmonic imaging and detection of single exosomes. *Proc. Natl. Acad. Sci. U.S.A.* **115**, 10275–10280 (2018).
12. A. R. Halpern, J. B. Wood, Y. Wang, R. M. Corn, Single-nanoparticle near-infrared surface plasmon resonance microscopy for real-time measurements of DNA hybridization adsorption. *ACS Nano* **8**, 1022–1030 (2014).
13. R. Liu, X. Shan, H. Wang, N. Tao, Plasmonic measurement of electron transfer between a single metal nanoparticle and an electrode through a molecular layer. *J. Am. Chem. Soc.* **141**, 11694–11699 (2019).
14. J. J. Mock, D. R. Smith, S. Schultz, Local refractive index dependence of plasmon resonance spectra from individual nanoparticles. *Nano Lett.* **3**, 485–491 (2003).
15. J. A. Scholl, A. L. Koh, J. A. Dionne, Quantum plasmon resonances of individual metallic nanoparticles. *Nature* **483**, 421–427 (2012).
16. N. Darwish *et al*., Observation of electrochemically controlled quantum interference in a single anthraquinone-based norbornylogous bridge molecule. *Angew. Chem. Int. Ed. Engl.* **51**, 3203–3206 (2012).
17. F. Benz *et al*., Nanooptics of molecular-shunted plasmonic nanojunctions. *Nano Lett.* **15**, 669–674 (2015).
18. R. Esteban, A. G. Borisov, P. Nordlander, J. Aizpurua, Bridging quantum and classical plasmonics with a quantum-corrected model. *Nat. Commun.* **3**, 825 (2012).
19. K. J. Savage *et al*., Revealing the quantum regime in tunnelling plasmonics. *Nature* **491**, 574–577 (2012).

Downloaded at Palestinian Territory, occupied on December 12, 2021

www.manaraa.com

20. C. Ciracì *et al*., Probing the ultimate limits of plasmonic enhancement. *Science* **337**, 1072–1074 (2012).
21. S. F. Tan *et al*., Quantum plasmon resonances controlled by molecular tunnel junctions. *Science* **343**, 1496–1499 (2014).
22. M. J. Rust, M. Bates, X. Zhuang, Sub-diffraction-limit imaging by stochastic optical reconstruction microscopy (STORM). *Nat. Methods* **3**, 793–795 (2006).
23. P. Bon *et al*., Self-interference 3D super-resolution microscopy for deep tissue investigations. *Nat. Methods* **15**, 449–454 (2018).
24. X. Shan, U. Patel, S. Wang, R. Iglesias, N. Tao, Imaging local electrochemical current via surface plasmon resonance. *Science* **327**, 1363–1366 (2010).
25. J. J. Mock *et al*., Distance-dependent plasmon resonant coupling between a gold nanoparticle and gold film. *Nano Lett.* **8**, 2245–2252 (2008).
26. R. T. Hill *et al*., Plasmon ruler with angstrom length resolution. *ACS Nano* **6**, 9237–9246 (2012).
27. W. Wang, T. Lee, M. A. Reed, Mechanism of electron conduction in self-assembled alkanethiol monolayer devices. *Phys. Rev. B* **68**, 35416 (2003).
28. H. Yu, X. Shan, S. Wang, H. Chen, N. Tao, Molecular scale origin of surface plasmon resonance biosensors. *Anal. Chem.* **86**, 8992–8997 (2014).
29. V. Amendola, R. Pilot, M. Frasconi, O. M. Maragò, M. A. Iatì, Surface plasmon resonance in gold nanoparticles: A review. *J. Phys. Condens. Matter* **29**, 203002 (2017).
30. D. J. Wold, C. D. Frisbie, Fabrication and characterization of metal-molecule-metal junctions by conducting probe atomic force microscopy. *J. Am. Chem. Soc.* **123**, 5549–5556 (2001).
31. Z. Xie *et al*., Exceptionally small statistical variations in the transport properties of metal-molecule-metal junctions composed of 80 oligophenylene dithiol molecules. *J. Am. Chem. Soc.* **139**, 5696–5699 (2017).
32. V. Kravtsov, S. Berweger, J. M. Atkin, M. B. Raschke, Control of plasmon emission and dynamics at the transition from classical to quantum coupling. *Nano Lett.* **14**, 5270–5275 (2014).
33. W. Zhu *et al*., Quantum mechanical effects in plasmonic structures with subnanometre gaps. *Nat. Commun.* **7**, 11495 (2016).
34. A. D. Castañeda, N. J. Brenes, A. Kondajji, R. M. Crooks, Detection of microRNA by electrocatalytic amplification: A general approach for single-particle biosensing. *J. Am. Chem. Soc.* **139**, 7657–7664 (2017).
35. R. Tavallaie *et al*., Nucleic acid hybridization on an electrically reconfigurable network of gold-coated magnetic nanoparticles enables microRNA detection in blood. *Nat. Nanotechnol.* **13**, 1066–1071 (2018).
36. H. Schwarzenbach, N. Nishida, G. A. Calin, K. Pantel, Clinical relevance of circulating cell-free microRNAs in cancer. *Nat. Rev. Clin. Oncol.* **11**, 145–156 (2014).
37. H. Wang, Z. Tang, Y. Wang, G. Ma, N. Tao, Probing single molecule binding and free energy profile with plasmonic imaging of nanoparticles. *J. Am. Chem. Soc.* **141**, 16071–16078 (2019).
38. T. Wang, C. A. Nijhuis, Molecular electronic plasmonics. *Appl. Mater. Today* **3**, 73–86 (2016).

Downloaded at Palestinian Territory, occupied on December 12, 2021

www.manaraa.com